Engineering xxx (xxxx) xxx

Contents lists available at ScienceDirect

Engineering

journal homepage: www.elsevier.com/locate/eng

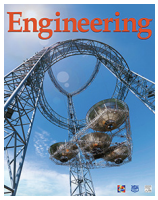

Research
Unconventional and Intelligent Oil & Gas Engineering—Review

Transport in Nanoporous Media

Weiyao Zhu *, Bin Pan, Zhen Chen, Wengang Bu, Qipeng Ma, Kai Liu, Ming Yue

School of Civil and Resource Engineering, University of Science and Technology Beijing, Beijing 10083, China

ARTICLE INFO

Article history:
Received 7 February 2023
Revised 17 April 2023
Accepted 16 May 2023
Available online xxxx

Keywords:
Transport in nanoporous media
Multi-phase fluid dynamics
Nonlinear flow mechanisms
Nonlinear flow conservation equations
Interfacial forces
Molecular dynamics simulation

ABSTRACT

Fluid flow at nanoscale is closely related to many areas in nature and technology (e.g., unconventional hydrocarbon recovery, carbon dioxide geo-storage, underground hydrocarbon storage, fuel cells, ocean desalination, and biomedicine). At nanoscale, interfacial forces dominate over bulk forces, and nonlinear effects are important, which significantly deviate from conventional theory. During the past decades, a series of experiments, theories, and simulations have been performed to investigate fluid flow at nanoscale, which has advanced our fundamental knowledge of this topic. However, a critical review is still lacking, which has seriously limited the basic understanding of this area. Therefore herein, we systematically review experimental, theoretical, and simulation works on single- and multi-phases fluid flow at nanoscale. We also clearly point out the current research gaps and future outlook. These insights will promote the significant development of nonlinear flow physics at nanoscale and will provide crucial guidance on the relevant areas.

1. Introduction

Fluid flow at nanoscale is everywhere in our daily life, which is closely related to various nature and technologies. For example, it determines hydrocarbon distribution characteristics/recovery efficiencies in unconventional reservoirs [1–10]; soil contamination/remediation at subsurface [11–13]; gas (H_2, CO_2, and CH_4) geo-storage capacities, leakage risks, and injection/withdrawal efficiencies [14–22]; electrochemical devices and fuel cells performances [23–25]; drug delivery and targeted therapy [26,27]; wastewater processing [28–30]; as well as material synthesis [31]. At nanoscale, interfacial forces are dominant over bulk forces, and nonlinear characteristics play important roles; thus, conventional theory is no longer applicable [32]. During the past decades, massive studies in terms of experiments, theories, and simulations have been reported on this topic, while a critical review is still lacking, which has seriously limited the fundamental understanding of this area.

On this premise, experimental, theoretical, and simulation works on single- and multi-phases fluid flow at nanoscale were systematically reviewed. The current research gaps and future outlook were also clearly pointed out. This comprehensive review may provide a crucial source for the development of nanoscale nonlinear flow physics and a valuable reference for relevant fields.

2. Single-phase flow

2.1. Experiments

Since Sumio Iijima invented carbon nanotubes (CNTs) in 1991 [33], many researchers have studied single-phase liquid flow inside CNTs. For example, Majumder et al. [34] inserted thousands of multiwalled CNTs (with an internal radius of 7 nm and an area density of 5×10^{10} cm^{-2}) parallelly inside a solid polystyrene membrane to study fluid dynamics inside them; the following was found: ① liquids (water, ethanol, isopropanol, hexane, and decane) flow rates are four to five orders of magnitude faster than the conventional fluid flow predictions; and ② the slip lengths are as high as 3.4–68.0 mm, see Table 1. However, these interesting experimental investigations were unable to indicate the underlying mechanisms of this abnormal phenomenon. From the perspective of molecular dynamics (MD) simulations, Skoulidas et al. [35] thought that the intermolecular forces between the gas and CNT wall are responsible for the observed acceleration behavior.

Subsequently, Holt et al. [36] developed a micro-electrical–mechanical system, fabricated a CNT (with a radius of 2 nm) array, filled the gap between CNTs and succeeded in monitoring the *in-situ* fluid dynamics. The results demonstrated that ① the gas flow rate is approximately two orders of magnitude larger than the classic Knudsen diffusion predictions; ② the water flow rate is approximately 3–4 orders of magnitude larger than the Hagen–Poiseuille

* Corresponding author.
E-mail address: weiyaook@sina.com (W. Zhu).

https://doi.org/10.1016/j.eng.2023.05.014

Table 1
Pressure-driven flow parameters of different liquids through aligned multi-wall CNTs.

Liquid	Initial permeability ($cm^3 \cdot cm^{-2} \cdot min \cdot bar$)	Observed flow velocity ($cm \cdot s^{-1} \cdot bar^{-1}$)	Expected flow velocity ($cm \cdot s^{-1} \cdot bar^{-1}$)	Slip length (mm)
Water	0.580	25.00	0.00057	54.0
	1.010	43.90	0.00057	68.0
	0.720	9.50	0.00015	39.0
Ethanol	0.350	4.50	0.00014	28.0
Isopropanol	0.088	1.12	0.00077	13.0
Hexane	0.440	5.60	0.00052	9.5
Decane	0.053	0.67	0.00017	3.4

1 bar = 10^5 Pa.

(H–P) predictions; and ③ the slip length is up to 1400 nm, see Table 2.

However, in the abovementioned experimental studies, the CNT density across the influx area could not be accurately quantified, which might cause experimental errors to some extent [37]. Furthermore, capillary end and inertial effects are almost unavoidable for these CNTs with lengths of several micrometers. Some researchers thought that the atomic-scale surface roughness of CNTs and the ordered distribution of fluid molecules at the sub-nanometer scale are responsible for the enhanced fluid flow rate [34]. Another possible reason might be the problematic experimental designs, namely before the fluid flows into and out of the CNTs, the dramatic cross-sectional area change will lead to a significant fluid rate increase, Fig. 1. However, this hypothesis has not yet been strictly validated by experiment or theory – which is still a world-class challenge.

CNT membrane separation technology is widely applied in wastewater treatment. Tofighy and Mohammadi [38] fabricated a novel adsorptive membrane to remove nickel ions from water. Wang et al. [39] applied nanocomposite membranes containing single-walled CNTs (SWCNTs) and multiwalled CNTs (MWCNTs) to remove pharmaceuticals and personal care products (PPCPs) in water. They noted that the reduced electrostatic repulsion or formation of hydrogen bonds makes the removal of neutral PPCP molecules greater than that of ions.

With the rapid development of material fabrication and advanced imaging, micro- and nanofluidics have become important platforms to explore the fundamental physics of fluid flow at micro- and nanoscales [40–44]. Through these platforms, nonlinear phenomena are clearly observed as follows. Cui et al. [45] found that when the straight tube radius ranges from 3 to 10 μm, the relationship between the flow rate and the pressure difference for isobutanol and carbon tetrachloride starts to deviate from the H–P equation. Furthermore, the H–P equation was modified to consider an exponential relationship between viscosity and pressure to fit the experimental data with theoretical estimations [45]. Choi et al. [46] adopted a chemical approach to alter the wettability of channels (with depths of 1–2 μm) for investigation of the wettability impact, observing that slip flow exists at hydrophobic surfaces, for example, the slip length is linear with the shear rate, and the slip length is up to 30 nm at a shear rate of 10^5 s^{-1}. However, for a hydrophilic surface, uncertainty about the presence or

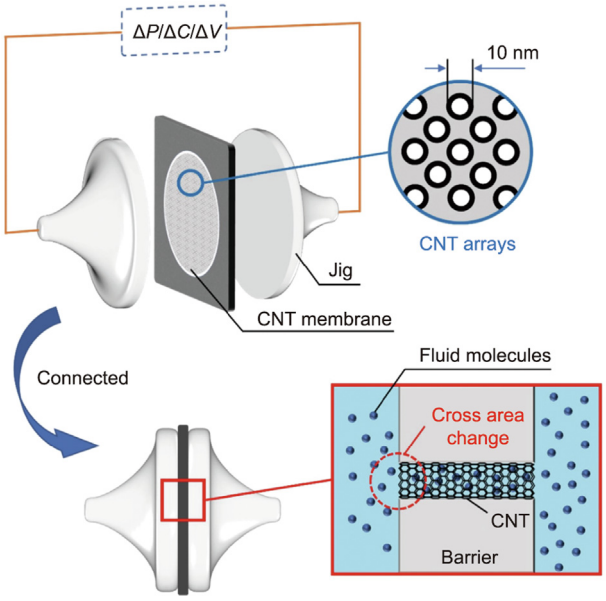

Fig. 1. Illustration of the experimental setup causing the hypothesized error possibly responsible for the enhanced flow rate in CNTs. $\Delta P/\Delta C/\Delta V$: pressure/concentration/voltage difference.

absence of slip phenomena remains [46]. Based on the confocal microparticle imaging velocity technique, Lumma et al. [47] found the existence of a slip phenomenon in a straight tube with a radius of 100 μm, and the underlying reason is attributed to the electrostatic forces of particles, consistent with a later study by Jin et al. [48]. Based on a surface force apparatus, Horn et al. [49] measured the slip length of an ideally elastic liquid on an ideally flat solid surface, observing that the liquid extrusion rate is far larger than the theoretical prediction value. This indirectly indicates the presence of a slip phenomenon with a slip length of 30–50 nm (which is approximately 1–2 orders of magnitude larger). The underlying mechanisms can be attributed to the coupled influences of the rod-climbing effect, fluid and solid properties, and experimental approaches.

Very recently, Shen et al. [50] investigated the dynamics of single-phase gas (N_2) flow in quartz microtubes and aluminum

Table 2
Comparison between the experimental and theoretical flow rates for air and water in various CNT membranes.

Membrane	Pore diameter (nm)	Pore density (cm^{-2})	Thickness (μm)	Enhancement over the Knudsen model (minimum)	Enhancement over no-slip, hydrodynamic flow (minimum)	Calculated minimum slip length (nm)
DWNT 1	1.3–2.0	$\leq 0.25 \times 10^{12}$	2.0	40.0–120.0	1500.0–8400.0	380.0–1400.0
DWNT 2	1.3–2.0	$\leq 0.25 \times 10^{12}$	3.0	20.0–80.0	680.0–3800.0	170.0–600.0
DWNT 3	1.3–2.0	$\leq 0.25 \times 10^{12}$	2.8	16.0–60.0	560.0–3100.0	140.0–500.0
Polycarbonate	15.0	6×10^8	6.0	2.1	3.7	5.1

DWNT: double-walled CNTs.

oxide nanoporous membranes (Table 3). The experimental results demonstrated that ① the gas flow rate is approximately one order of magnitude larger than the H–P theoretical predictions (due to Knudsen diffusion and slip flow); and ② the slip length decreases with increasing pressure difference and tube radius (Fig. 2) [50].

The abovementioned experimental studies were all based on ideal capillary (bundle) flow, without considering the complexity of actual porous media. In 1944, nanoporous glass (Vycor) was used to study the flow dynamics of a single-phase of water or acetone by Nordberg for the first time [51]. The relationship between the flow rate and the pressure difference appeared to be linear, while details about the experimental techniques and data points were not clearly reported in this work [51]. Afterward, Debye and Cleland [52] investigated the flow dynamics of a series of liquid hydrocarbons in Vycor (with a pore radius of 4.0 nm and a bulk thickness of 1.1 mm) and observed obvious nonlinear characteristics, namely, the coefficient of the flow rate to pressure difference is continuously changing, and an exponential correlation between the permeability and viscosity exists (Fig. 3). However, to quantify these experimental results, the authors simplified the nonlinear physics and assumed the presence of an adsorption layer, namely, a layer of immobile liquid molecules are adsorbed on the surface of nanopores, and that H–P flow is still valid from this layer inward, thus reducing the effective radius for fluid flow. However, intrinsically, a series of interfacial forces (e.g., capillary force, van der Waals forces, disjoining pressure, and line tension) dominate at nanoscale, and fluid properties (e.g., viscosity and density) deviate from their macroscopic properties, all of which cause nonlinear flow physics.

However, the above investigations of single-phase flow in Vycor were all performed under ambient conditions. Very recently, Gruener et al. [53] investigated the dynamics of water and hexane flow in Vycor at high pressure and high temperature, obtaining similar physics as Ref. [52]. More interestingly, after Vycor became hydrophobic through alkylation, water was unable to enter Vycor even at pressures up to 7 MPa.

2.2. Theory

Commonly, there are two methods to describe the strong interfacial interactions between fluid and solid at nanoscale (i.e., viscosity modification and force field modification).

In terms of viscosity modification, You et al. [54] and Wang et al. [55] considered the molecular interactions to establish an effective viscosity function inside two parallel plates (Eq. (1)) and a circular tube (Eq. (2)),

$$\mu_e = \mu_b + \frac{\xi_1}{(H-y)^{n_1}} + \frac{\xi_2}{(H+y)^{n_2}} \tag{1}$$

$$\mu_e = \mu_b + c\frac{\sqrt{A_s A_w} - A_w}{r} \tag{2}$$

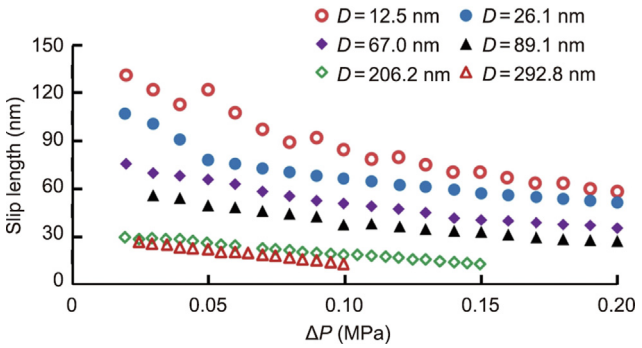

Fig. 2. Nitrogen slip length as a function of the pressure difference and alumina membrane diameter. Reproduced from Ref. [50] with permission.

where μ_e and μ_b are the effective viscosity and bulk viscosity, respectively; ξ and n are determined by the properties of fluid and solid; H is the half height of the channel; y is the vertical distance from the pore wall to the channel center; c is the viscosity enhancement factor; A_s and A_w are the Hamaker constants for the fluid and the wall, respectively; and r is the distance from the wall.

Thomas and McGaughey [56] considered the weights of the interfacial and bulk fluid viscosities, thus developing an effective viscosity model (Eq. (3)),

$$\mu_e = \mu_i \frac{A_i}{A_t} + \mu_b \frac{A_b}{A_t} \tag{3}$$

where μ_i is the interfacial viscosity and A_i, A_b, and A_t are the interfacial, bulk, and total areas, respectively. However, μ_i and A_i are difficult to determine, which has limited the widespread application and reliability of this model.

Wu et al. [57] developed an empirical correlation between the interfacial viscosity and contact angle (θ) based on experimental data and MD simulations (Eq. (4)).

$$\frac{\mu_i}{\mu_b} = -0.018\theta + 3.25 \tag{4}$$

This model was derived semi-empirically and is consistent with almost 50 literature studies, while it is unable to rigorously reflect the underlying physical significance.

Furthermore, Zhang et al. [58] considered the influences of interfacial forces on the interfacial viscosity and combined kinetic theory to derive a new viscosity model (Eq. (6)),

$$\frac{\mu_i}{\mu} = \exp\left(\frac{\prod_h \pi\sigma_{LS}^3}{6kT}\right) \text{ and } \frac{\mu_b}{\mu} = \exp\left(\frac{\prod_h \pi\sigma_{LL}^3}{6kT}\right) \tag{5}$$

$$\mu_e = \frac{\int \mu_i dA_i + \int \mu_b dA_b}{A_t} \tag{6}$$

where μ is the macroscale viscosity; $\prod_h$ is the disjoining pressure; σ_{LS} and σ_{LL} are the liquid–solid and liquid–liquid Lennard–Jones

Table 3
Information about the quartz microcapillary and alumina membrane used.

Material	Diameter	Porosity (%)	Quantity ($N{\cdot}a^{-1}$)[a]	Pore length	Length–diameter ratio
Quartz microcapillary	6.42 μm	100.00	1.0	4.51 cm	7025
Quartz microcapillary	14.50 μm	100.00	1.0	6.54 cm	4507
Lumina membrane	12.50 nm	8.30	2.1×10^{11}	45.00 μm	3589
Alumina membrane	26.10 nm	22.20	1.3×10^{11}	56.40 μm	2165
Alumina membrane	67.00 nm	26.10	2.3×10^{10}	88.10 μm	1315
Alumina membrane	89.20 nm	31.70	1.6×10^{10}	93.70 μm	1051
Alumina membrane	206.20 nm	31.40	3.0×10^{9}	56.40 μm	274
Alumina membrane	292.80 nm	39.30	1.8×10^{9}	88.10 μm	301

[a] $N{\cdot}a^{-1}$: number of pores per unit area.

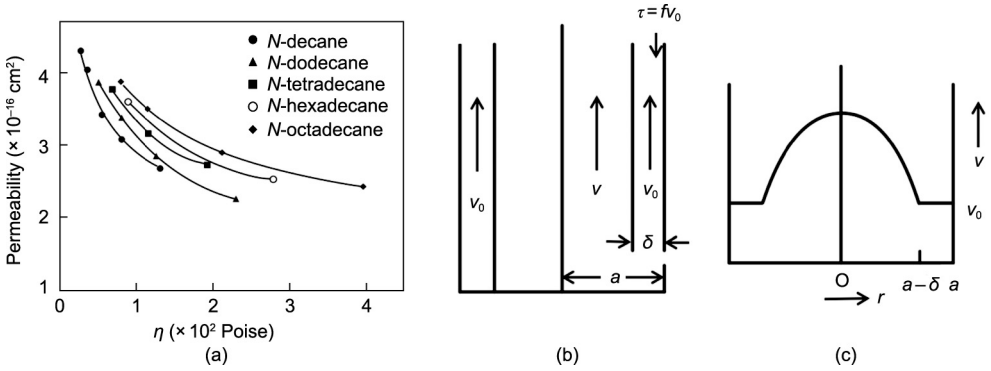

Fig. 3. (a) Permeability of Vycor as a function of hydrocarbon viscosity; (b) schematic of flow postulated for small capillaries; (c) velocity profile across the capillary. Reproduced from Ref. [52] with permission. 1 Poise = 0.1 Pa·s. v_0: the slip velocity; τ: the frictional stress; f: the friction factor; a: the cylindrical capillary radius; δ: the thickness of the layer adsorbed at the wall; v: the velocity in the inner cylinder of radius $(a-\delta)$; r: the coordinate.

distance parameters, respectively; k is the Boltzmann constant; and T is the temperature.

In terms of force field modification, the interfacial interactions are added as an extra acceleration term ($\boldsymbol{g}$) into the Navier–Stokes equation (Eq. (7)),

$$\rho(\boldsymbol{u}\cdot\nabla)\boldsymbol{u} = -\nabla p + \mu\nabla^2\boldsymbol{u} + \frac{1}{3}\mu\nabla(\nabla\cdot\boldsymbol{u}) + \boldsymbol{g} \tag{7}$$

where ρ is the fluid density; $\boldsymbol{u}$ is the velocity; p is the pressure.

For example, Zhang et al. [59] considered the influence of electrostatic forces (f_e) (Eq. (8)), and Zhang et al. [60] considered the influence of van der Waals forces (f_V) (Eq. (9)).

$$f_e = \frac{zq\varphi}{\lambda}e^{\frac{1}{\lambda}(r-R)} \tag{8}$$

$$f_V = -\frac{A_H R\left[\left(R^4+r^4+14R^2r^2\right)E_c\left(\frac{r}{R}\right)+\left(7r^4-R^4-6R^2r^2\right)K_c\left(\frac{r}{R}\right)\right]}{2\pi r\left(6R^4r^4-4R^6r^2-4R^2r^6+r^8+R^8\right)} \tag{9}$$

where z is the valence; q is the charge density; φ is the potential difference; λ is the electrical double layer thickness; A_H is the Hamaker constant; R is the microtube radius; and K_c and E_c are type I and II elliptic integrals, respectively.

In terms of the suppressed transport phenomena at nanoscale, it is reasonable to use the intermolecular forces for the corresponding interpretations [61,62]. However, it is also common to use the slip flow boundary condition (Eq. (10)) to explain the enhanced transport phenomena [34]. Davidson and Xuan [63] established a thermo–electro–hydrodynamic model and discussed the effect of slip on electrokinetic energy conversion in nanochannels. The electrokinetic device performance can be enhanced in nanochannels with a high ratio of the slip length to channel height. Jeong et al. [64] investigated the Couette flow in a nanochannel by combining the numerical solutions from the continuum region and the particle region. They indicated that the no-slip condition can be used only when the channel height is sufficiently large.

$$u_s = b\left.\frac{\partial u_x}{\partial z}\right|_w \tag{10}$$

where u_s is the slip flow rate; b is the slip length, which is a constant; u_x is the flow rate parallel to the tube surface; z is the location along the normal axis; and $\partial u_x/\partial z$ is the shear rate. Thus, the modified H-P equation inside a straight CNT will be

$$Q = \frac{\pi R^4}{8\mu_e}\frac{\Delta p}{L}\left(1+\frac{4b}{R}\right) \tag{11}$$

where Q is the actual flow rate; L is the tube length.

Furthermore, Huang et al. [65] derived a relationship between the slip length and the contact angle (Eq. (12)),

$$b = \frac{C}{(\cos\theta+1)^2} \tag{12}$$

where C is a constant. For a hydrophilic CNT, there is no slip flow, while for a hydrophobic CNT, the slip flow phenomena become more significant.

2.3. Simulation

MD simulation is almost the most popular technique to simulate fluid flow at nanoscale (especially in CNTs) and to compare the results with the H–P theory. For example, Hanasaki and Nakatani [66] investigated the dynamics of water transport in a CNT with a radius of 0.8–2.7 nm and a length of 6.14 nm. The simulation results showed that the front velocity profile is piston-like, different from the parabolic shape of the H–P flow; thus, water has probably started to demonstrate non-Newtonian characteristics inside the interfacial region. This predicted piston-like velocity profile is qualitatively consistent with the results of Joseph and Aluru [67], where water flows inside a hydrophobic CNT with a diameter of 1.6 nm. Furthermore, the simulated water flow rate is approximately three orders of magnitude larger than the H–P predictions, while on the same order of magnitude as that in the experimental study by Majumder et al. [34]. The underlying reasons for the enhanced flow rate are again briefly attributed to the ideally smooth surface of CNTs, while how to quantify this surface roughness mathematically remains unknown. Later, Wang et al. [68] systematically investigated the kinetics of octane in a 5.24 nm nanopore. The velocity profile of octane was parabolic inside the SiO_2 plate (Fig. 4). Furthermore, an approximate slip length of 2.5 nm was estimated to fit the simulation data. In contrast, a good fit could not be achieved if only the effect of the bulk viscosity or apparent viscosity was considered (Fig. 4). However, once again, the underlying physics remain unclear.

Wang et al. [69] further compared the velocity profile of CH_4 in graphene, quartz, and calcite nanopores (Fig. 5). The results demonstrated that the CH_4 velocity profile is less parabolic for graphene than for quartz, which is less parabolic than that for calcite. The underlying mechanisms for this difference are attributed to different surface roughness values and intermolecular interactions.

Recently, Wu et al. [70] systematically investigated the impact of wettability on water transport inside CNTs with radii of 1.360–2.034 nm at various temperatures. For hydrophilic conditions, the water flow rate is approximately 30% smaller than the

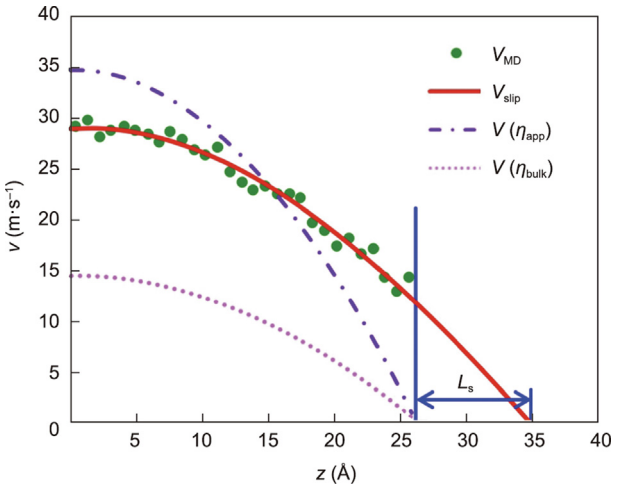

Fig. 4. Velocity profiles of *n*-octane in a 5.24 nm quartz nanopore. The red solid line is a parabolic velocity profile (V_{slip} estimated by a slip model) fit to the velocity profile (V_{MD}) predicted by the molecular dynamics simulation. L_s: the slip length; $V(\eta_{app})$ and $V(\eta_{bulk})$: predicted from the no-slip H–P equation with the apparent viscosity and bulk viscosity, respectively; *z*: the coordinate; *v*: the velocity. Reproduced from Ref. [68] with permission.

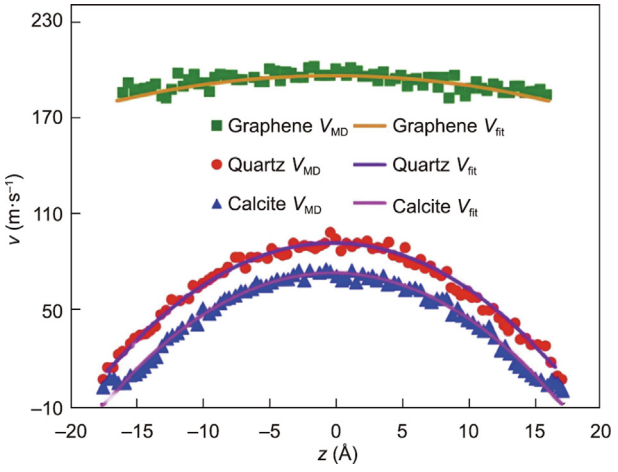

Fig. 5. Velocity profiles of CH_4 in graphene, quartz, and calcite nanopores. V_{fit}: the parabolic fitting to the simulated velocities. Reproduced from Ref. [69] with permission.

H–P predictions; in contrast, for hydrophobic conditions, the water flow is at least four orders of magnitude larger than the H–P predictions. However, the authors did not propose any physical or theoretical model to explain these results.

In terms of electrokinetic flow, Movahed and Li [71] performed a numerical study of electrokinetic transport through a three-dimensional nanotube in which the Boltzmann distribution of ions is inapplicable. The Poisson–Nernst–Plank equation, Navier–Stokes equation, and continuity equations were integrated and solved. The results showed that the electric potential field, ionic concentration field, and velocity field are determined by the nanochannel size.

Han and Chen [72] investigated the effects of the width and wall structure of the nanochannel on ion enrichment by combining the Poisson–Nernst–Plank equations and Navier–Stokes equation. When the nanochannel width decreases, the peak concentration and the peak voltage increase under the same voltage. The peak concentration is the highest in a nanochannel of the square wave wall structure.

Hsu et al. [73] proposed a modified continuum model to explain two phenomena that are not observed in microchannels but demonstrated in MD simulations: ① a decrease in the average electroosmotic mobility at a high surface charge density and ② a decrease in the channel conductance at high salt concentrations as the surface charge is increased. Their model improved the previous electric double layer model and reproduced these nanochannel-specific phenomena.

Mo and Hu [74] investigated the fluid flow and heat transfer within a two-parallel-plate microchannel considering the surface chemical reaction. The chemical reaction was affected by the pH and ionic concentration; thus, the flow was also influenced. When considering the slip boundary, the Nusselt number and dimensionless flow rate decrease by 12% and 50%, respectively.

Li et al. [75] studied the ion transport, fluidic flow, and heat transfer in nanochannels considering the electroviscous effect. Based on numerical simulation, the results showed that the channel height can bring relative errors of 50% and 80% to the local ionic concentration and potential, respectively. The reason is that the electric double layers overlap when the channel is narrow.

Understanding the physical and chemical behavior in micro/-nanopores is of great significance for improving the injection production efficiency. Zhang et al. [76] investigated the dependence of the competitive adsorption of C1–C2–C3 and C1–C2–C3–CO_2 mixtures on rock properties, pore size, and fluid composition by conducting grand canonical Monte Carlo simulations. In organic pores, the results showed that C1 can be recovered, whereas C2 and C3 are trapped. CO_2 injection into organic pores performs well in hydrocarbon recovery. Li and Sun [77] quantitatively evaluated CO_2-enhanced CH_4 recovery by using MD simulation. They found that CH_4 uptake is inhibited by increasing water and ethane contents. Under a high pressure, the efficiency of CH_4 displacement by CO_2 can be increased when the moisture content is above 3 wt%. Through MD simulation, Hong et al. [78] studied the competitive adsorption of asphaltene and *n*-heptane on quartz surfaces. Due to strong interfacial energy and polyaromatic ring interactions, asphaltene is more easily adsorbed on the quartz surface. The surface hydroxyl groups of quartz substrates affect asphaltene adsorption, resulting in enhancement of the oil flux through SiO_2 nanopores.

Gas transport in pores is crucial in the gas storage process. In addition, gas geo-storage is related to physisorption controlled by weak van der Waals forces [79]. Sorption includes surface adsorption, absorption, and capillary condensation [80]. Due to their large internal surface area, nanopores have a greater gas storage capacity [81]. By using MD simulation, Wu and Zhang [82] investigated the gas flow behavior considering the adsorption in nanochannels consisting of illite and graphene. The results showed that a velocity oscillation exists along the cross-section, and the total gas flux varies with increasing or decreasing absorption.

In the field of soil remediation, Ali et al. [83] investigated the impacts of NaCl, KCl, and $MgCl_2$ on the structure and dynamics of water at the calcite interface by MD simulation. In the first and second hydration layers, the well-organized structure of oxygen atoms is broken by these ions, with KCl having the largest effect. Zhang et al. [84] used MD simulation to study the physical chemical process in pollutant removal by activated carbons (ACs). Deprotonated cyclohexanoic acid (DCHA) and heptanoic acid (DHA) were the research objects. The results indicated that the hydrophilic head groups of both DCHA and DHA formed hydrogen bonds with —OH groups. The strong water film greatly reduces the adsorption of DCHA and DHA.

In summary, previous researchers mainly focused on the velocity magnitude and profile at nanoscale using MD simulations and numerical simulations and attempted to explain these simulation results based on the surface roughness and wettability. However,

thus far, all the work has been unable to uncover the underlying fundamentals.

3. Multi-phase flow

3.1. Experiments

Many experimental investigations on multi-phase flow (including spontaneous and forced imbibition; drainage) in nanoporous media, for example, CNTs, Vycor, membranes, and rocks, have been reported. Specifically, in terms of the capillary rise dynamics inside straight nanochannels, the spontaneous imbibition height and square root of time have been demonstrated to show a favorable linear relationship, regardless of the fluid type (water, ethanol, and isopropanol) or channel width (27, 50, and 73 nm) [85]. Li et al. [86] investigated the pore-scale mechanisms of surfactant (Gemini RF03) enhanced oil recovery (EOR) inside oil–wet quartz tubes and concluded that the coupled functions of the Marangoni effect, wettability alteration and interfacial tension reduction are responsible for EOR.

The Patrick Huber research group from Hamburg University of Technology systematically investigated spontaneous imbibition dynamics in Vycor. For example, Huber et al. [87] observed a good linear relationship between the spontaneous imbibition mass and square root of time for water, C15 and C24 in Vycor. Similar to the single-phase flow in Vycor, the authors herein also assumed that the effective radius for fluid flow is reduced by one molecular adsorption layer and that from this layer inward, the classic Lucas–Washburn (L–W) equation is valid. Furthermore, Gruener and Huber [88] investigated the influence of temperature on Vycor (with dominant pore radii of 7 and 10 nm) (Fig. 6). A higher temperature can cause faster spontaneous imbibition, which is attributed to the freezing function at the front. Furthermore, Gruener et al. [89] combined gravity analysis and optical and neutron imaging to explore the influence of the hydrocarbon chain length on the spontaneous imbibition dynamics (Fig. 7), finding that ① when the carbon number is 60, the observed spontaneous imbibition rate is larger than the predicted L–W rate, indicating the presence of slip flow or shear viscosity reduction; and ② with increasing spontaneous imbibition distance, the front roughness also gradually increases.

Although Vycor is an ideal material to investigate spontaneous imbibition physics in nanoporous media, its intrinsic hydrophilicity is not always applicable in nature. As carbon materials became increasingly popular in energy and environmental areas, Pan et al. [90,91] started to investigate the dynamics of water and silicon oil spontaneous imbibition in nanoporous carbon scaffolds (Fig. 8). For nanoliter droplet imbibition, as shown in Fig. 8(a) [90], the spontaneous imbibition rate has a linear relationship with time, and contact line pinning occurs, which is inconsistent with L–W theory. More interestingly, when the contact angle is larger than 90°, spontaneous imbibition dynamics can still occur, and the underlying mechanisms are attributed to capillary condensation. For bulk liquid spontaneous imbibition [91] in the absence of evaporation, as shown in Fig. 8(b), the spontaneous imbibition height has a linear relationship with the square root of time, following L–W theory. However, in the presence of evaporation, as shown in Fig. 8(c) [91], this relationship significantly deviates from linear. In contrast with Vycor, a clear adsorption layer was not observed in the nanoporous carbon scaffold.

For the purpose of understanding the gas–water two-phase flow physics in CNTs, the Yury Gogotsi research group used environmental scanning electron microscopy (ESEM) to systematically visualize the *in-situ* gas–water meniscus evolution dynamics and phase behavior (Figs. 9 and 10) [92,93]. For example, Gogotsi et al. [92] fabricated a multiwall CNT with two ends closed and 85% H_2O, 7% CO_2, and 7% CH_4 sealed inside. With increasing temperature, the liquid water gradually evaporated into the gaseous state, and the three-phase contact angle slightly increased (though still smaller than 90°), as shown in Figs. 9(a) and (b); furthermore, a liquid water film was found to form on the rough CNT internal surface, as shown in Fig. 9(c). Subsequently, Rossi et al. [93] successfully visualized the dynamics of a water film inside a carbon nanopipe with one end open, finding that the water film thickness increases as the pressure increases, while it decreases as the pressure decreases (although hysteresis is observed), as shown in Fig. 10.

Based on the ETEM and ESEM observations, the surface of the CNTs is hydrophilic, which is in significant contrast to common sense. However, how electron radiation will change the local temperature and surface properties of CNTs, thus impacting the observed results, remains unclear.

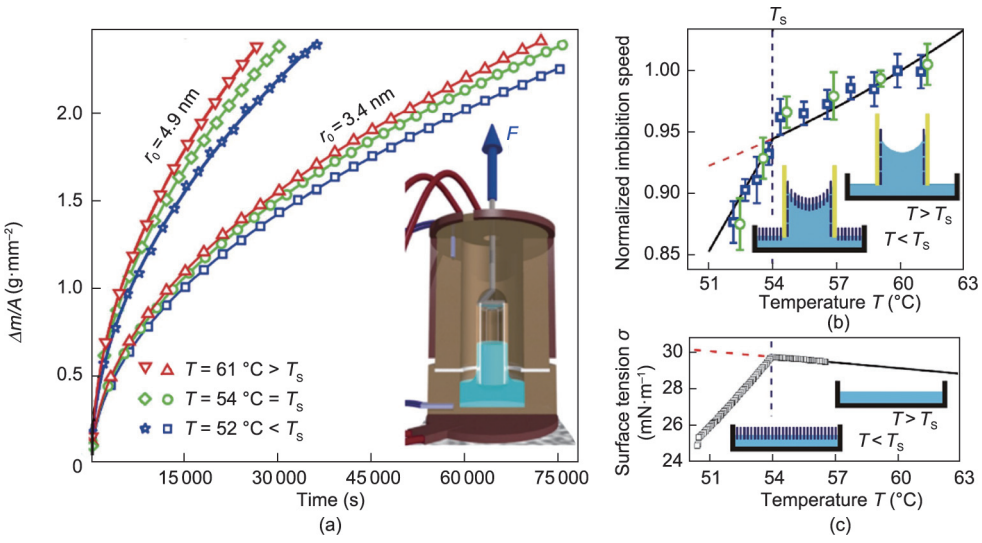

Fig. 6. (a) Spontaneous imbibition mass per unit area ($\Delta m/A$) as a function of time inside Vycor with various radii at various temperatures; (b) normalized imbibition speed as a function of temperature; (c) surface tension as a function of temperature. r_0 the mean pore radius; T_s is the temperature corresponding to abrupt temperature-slope change; Reproduced from Ref. [88] with permission.

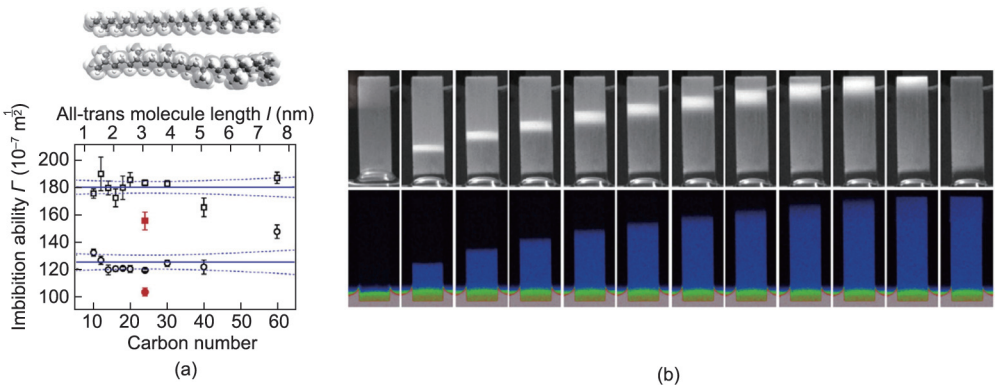

Fig. 7. (a) Liquid hydrocarbon spontaneous imbibition ability as a function of carbon number; and (b) spontaneous imbibition of *n*-tetradecane into Vycor with dimensions of 4.55 mm × 4.55 mm × 15.00 mm. Reproduced from Ref. [89] with permission.

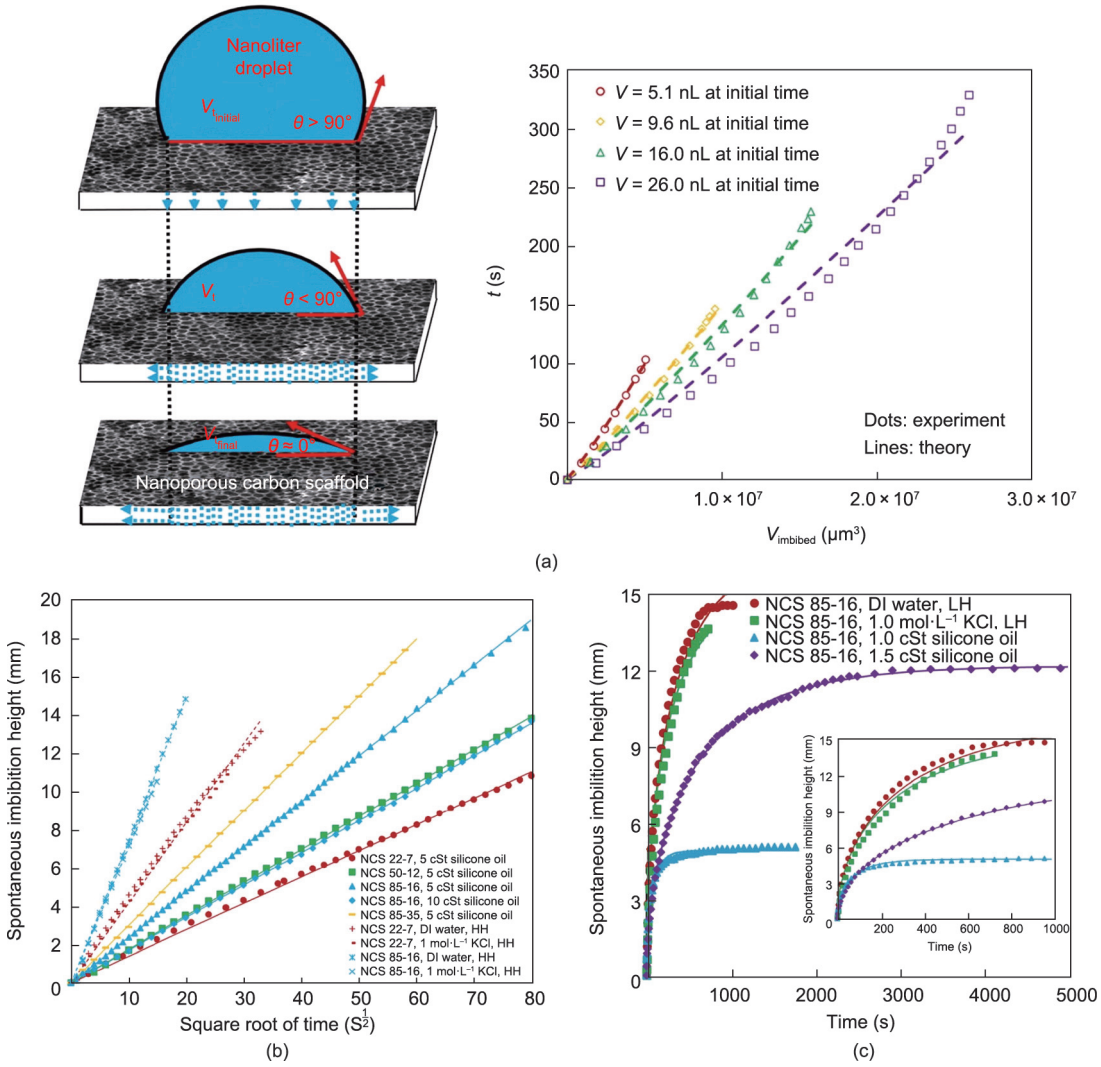

Fig. 8. (a) Spontaneous imbibition of nanoliter water droplets in hydrophobic nanoporous caron scaffolds; (b) spontaneous imbibition of bulk liquid in the absence of evaporation; (c) spontaneous imbibition of bulk liquid in the presence of evaporation. V_t: the droplet volume; NCS: the nanoporous carbon scaffold; V: the initial droplet volume; cSt: the unit of kinematic viscosity; DI: de-ionized; $V_{imbibed}$: the imbibed volume. HH: high humidity; LH: low humidity. (a) Reproduced from Ref. [90] with permission; (b, c) reproduced from Ref. [91] with permission.

Very recently, Anand et al. [94] succeeded in finding the existence of a water precursor film inside a silicone nanoporous network in liquid-phase TEM (Figs. 11(a)–(c)). More specifically, when the channel height was 230 nm, the deformation of silicon posts was not observed, as shown in Fig. 11(d); when the channel height was 285 and 380 nm, water–silicon interactions deformed

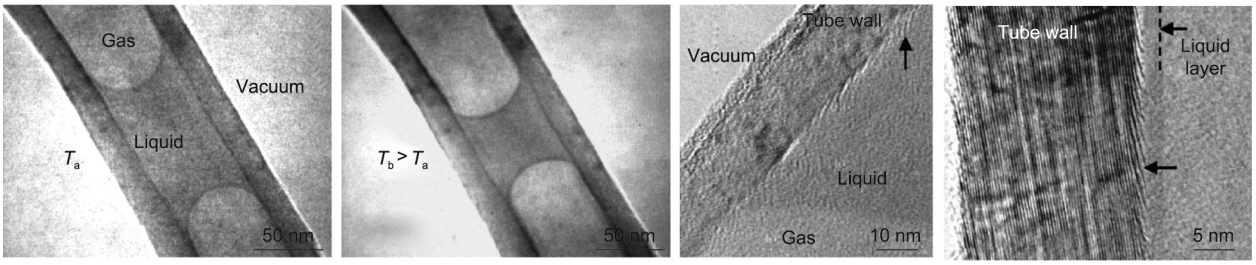

Fig. 9. (a, b) Gas–water two-phase flow physics at different temperatures, and (c) existence of a liquid film next to the rough surface, all visualized by ETEM. T_a: the initial temperature; T_b: the heating temperature. Reproduced from Ref. [92] with permission.

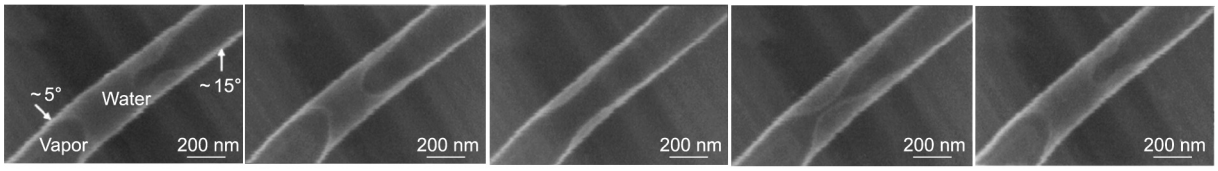

Fig. 10. Dynamic behavior of a water plug close to the open end of the tube at (a) 5.5 Torr (1 Torr = 133.322 Pa), (b) 5.8 Torr, (c) 6.2 Torr, (d) 5.8 Torr, (e) 5.7 Torr, all visualized by ESEM. Reproduced from Ref. [93] with permission.

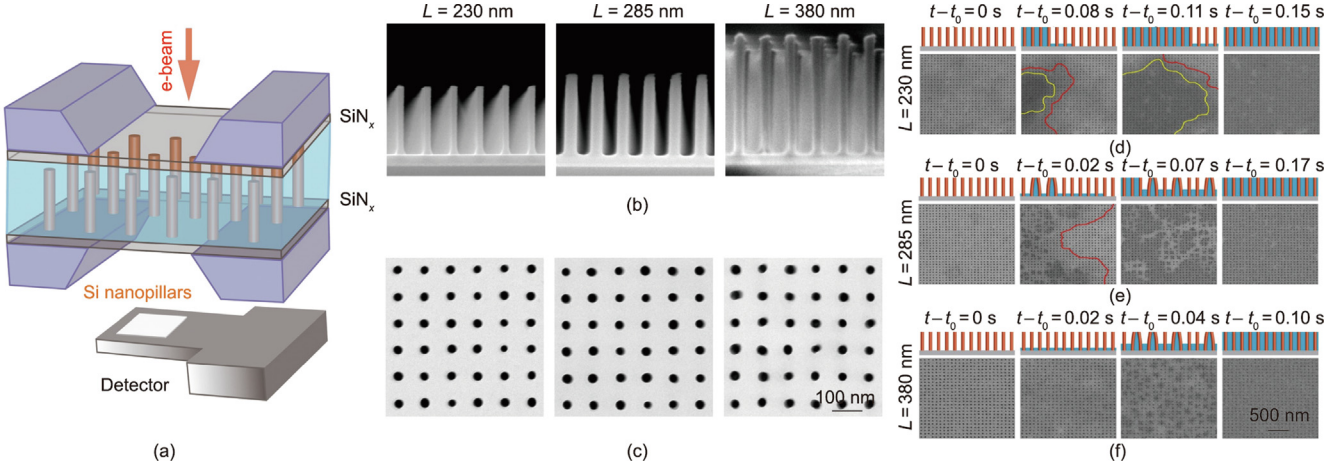

Fig. 11. (a) Experimental setup of the liquid-phase transmission electron microscope; (b) cross-sectional SEM; (c) top–down TEM images of the nanofluidic models; (d–f) water–silicone post interactions as a function of the post height. L: the hight of cylindrical Si nanopillars; t_0: the last frame where the surface was still completely dry during imaging. Reproduced from Ref. [94] with permission.

the silicon posts, while water filling recovered their original shape, as shown in Figs. 11(e) and (f).

Precise ionic transport through biomimetic nanochannels has been studied in biosensors and drug delivery devices [95]. Ferrati et al. [96] reported a nanochannel membrane with geometrically defined channels as small as 2.5 nm that achieves constant drug delivery *in vivo*. The *in vitro* and *in vivo* analysis of the membrane proved the flexibility of the technology. Romano-Feinholz et al. [97] used MWCNTs with diameters of 23 and 25 nm to study the drug delivery process and demonstrated the positive effects of these MWCNTs.

Micro/nanochannels can also be used to prepare membranes with flexible geometries. This flow-assembly technique is versatile and biologically friendly [98]. Shakeri et al. [99] presented a microfluidic device that can generate desired two-dimensional (2D) and one-dimensional (1D) gradients simultaneously. The feasibility of the microfluidic device was proven by finite element simulation. Based on the *in-situ* formation of biopolymer membranes, Gu et al. [100] developed [100] developed a microfluidic gradient generator. They analyzed the gradient-driven flow speed and showed that the measured velocity profiles are consistent with those generated by hydrodynamic models.

In the areas of shale oil and gas, scholars have performed a large amount of work on the physics of gas–water and gas–oil transport in natural rocks and artificial models. Wang et al. [101] observed the oil/gas phase behavior in nanoporous rocks by applying nanofluidic devices to visualize the phase change of alkane. They reported that the vaporization of the liquid phase is much weaker in nanochannels than in microchannels. To study the spontaneous imbibition in ultra-tight nanoporous media, Akbarabadi et al. [102] constructed a new device consisting of a miniature fluid-injection module and a high-resolution X-ray imaging system. They first provided experimental evidence of oil/brine imbibition in ultra-tight rock at the pore scale.

For visual micro/nano multi-phase flow experiments, the glass porous media micromodel is crucial and widely used. Xu et al.

[103] developed a special fabrication method for glass micromodels. The real porous media and flow characteristics can be well represented by their micromodels. Deglint et al. [104] compared the macro- and microcontact angles of distilled water on different samples. The results indicated that the microcontact angles are significantly different from the macrocontact angles. The microcontact angles have a wider range and depend on the grain composition. Qiao et al. [105] investigated the unsteady-state gas–water flow in tight cores and discussed it through water layer theory and an effective flow radius model. They demonstrated the threshold for the onset of continuous nonwetting phase fluid intrusion (ISTP) in a gas displacement experiment. The water movement in the inner layer of the weakly bound water zone located in the narrow throats determines the criticality of gas intrusion when the injection pressure < ISTP.

For details, it is suggested to refer to previous review articles, for example, Refs. [106,107]. Several representative works contributed by our own research group will be introduced next.

To investigate the fundamental mechanisms of fracturing fluid loss in shale gas reservoirs, Pan et al. [1,108] developed a new method that can mitigate the influences of rock heterogeneity (Fig. 12(a)). The experimental results showed that osmotic pressure is an important mechanism for fracturing fluid loss, for example, for an organic-rich shale sample from the Canadian Duvernay formation, up to 13% fracturing fluid loss is caused by osmotic pressure (Fig. 12(b)).

Whether a threshold pressure gradient (TPG) exists in shale formations is still controversial [109–111]. The TPG is commonly believed to be a function of time and space, which is influenced by the rock properties, fluid saturation distribution, and fluid–rock

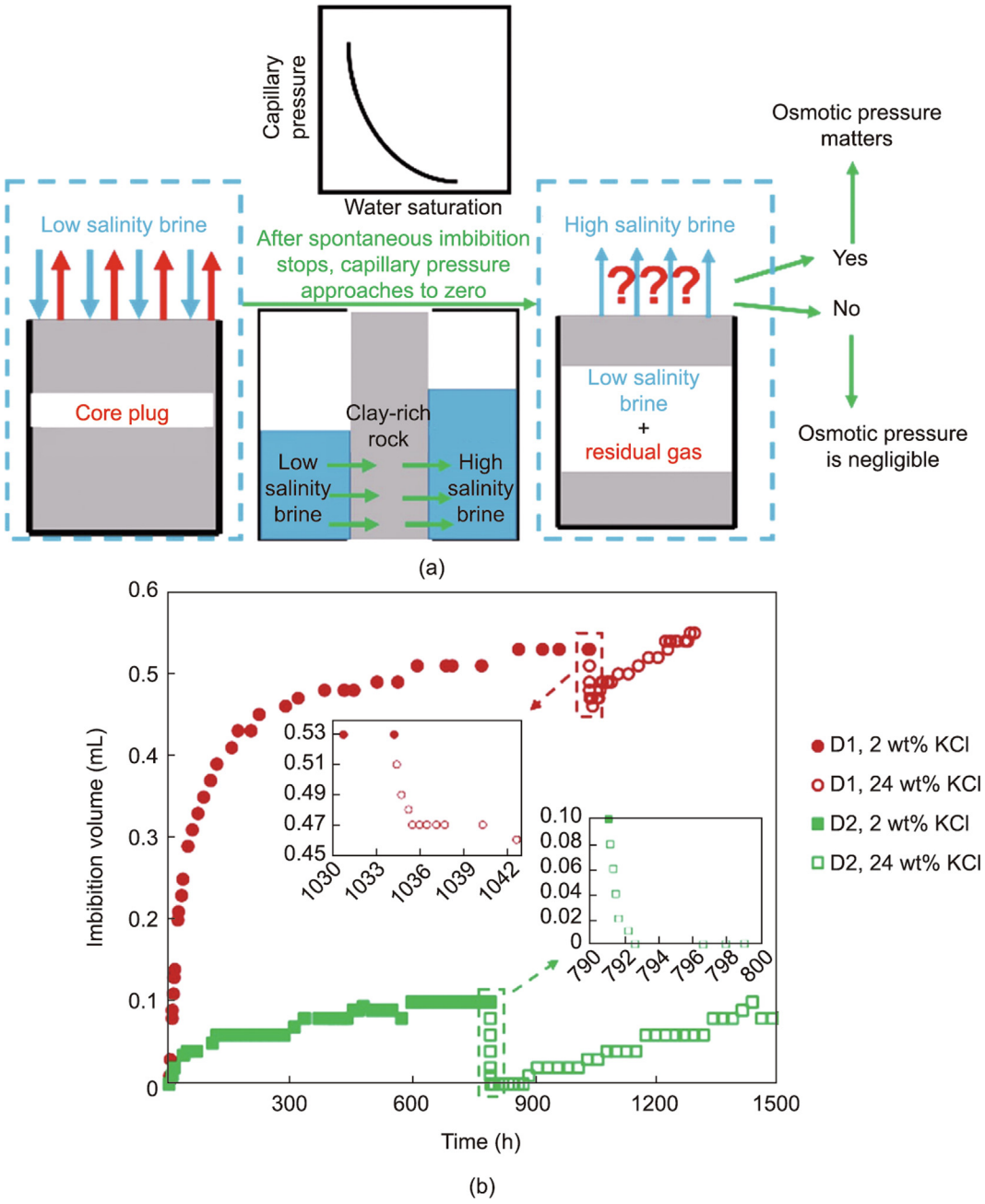

Fig. 12. (a) Schematic of the new experimental workflow for investigating the impact of osmotic pressure on the fracturing fluid loss in clay-rich unconventional reservoir samples; and (b) impact of osmotic pressure on spontaneous countercurrent imbibition in clay-rich Duvernay D1 and D2 samples. Reproduced from Ref. [1] with permission.

interactions. In addition, the relative permeability is an important parameter for two-phase flow and is a function of the pressure, temperature, saturation history, flow rate, wettability, and fluid properties [111]. However, measuring this parameter in tight and shale rocks is still a great challenge. In light of the current limitations of the underlying fundamentals, Zhu [112] considered multi-phase fluids as a mixed fluid and derived a thermodynamic equilibrium formula including interfacial evolution, mass transfer, and phase mixing, which is a valuable supplement to multi-phase flow theory.

3.2. Theory

To modify the conventional two-phase flow theory to accommodate the characteristics occurring at nanoscale, Zhang [113] made an appropriate modification to the force fields and derived a flow rate decrease coefficient η_V that includes the influences of van der Waals forces and compressibility (Eq. (13)),

$$\eta_V = -\frac{\kappa A_H}{6\pi R^2}\left[\frac{12}{5}\delta + 11 - \frac{16}{\delta} + \frac{4}{\delta^3} - 12\ln\delta\right] \tag{13}$$

where κ is the compressibility coefficient and δ is the thickness of a molecular layer.

For the process of water flooding for EOR, the flow rate is $u = u_P(1+\eta_V)$, where u and u_P are the actual and H–P predicted flow rates, respectively.

In contrast, Wang [114] made corresponding modifications to the viscosity term in the motion equation to describe the process of piston-like water flooding for the EOR process, as shown in Eq. (14):

$$\mu_i \frac{1}{r}\frac{d}{dr}\left[r\frac{d}{dr}(u_{wf} + \varsigma u_{wv})\right] = \frac{\Delta p}{L} \tag{14}$$

where u_{wf} is the water film flow rate; ς is the modification factor for the water vapor flow rate; and u_{wv} is the steam flow rate.

Prior to the derivation of Eq. (14), the authors made three assumptions, namely, the existence of water film adsorption (high viscosity region) on the hydrophilic tube surface, the occupation of gas in the center of the tube (slip flow region), and the sandwiching of bulk water (H–P flow region) between the water film and the gas (Fig. 13) [114].

However, Eqs. (13) and (14) did not consider the influence of spontaneous imbibition driven by capillary pressure. To address this, Zhang et al. [115] introduced a new model (Eq. (15)) to describe the process of gas–water spontaneous imbibition under the influence of a precursor film (Fig. 14). For a hydrophilic nanotube, the water precursor film can be formed by strong water–wall interactions, while the fluid dynamics in the internal region follow the L–W model very well,

$$L_t = L - (L_t + L_f)\frac{A_i\rho_i}{A_b\rho_b} \tag{15}$$

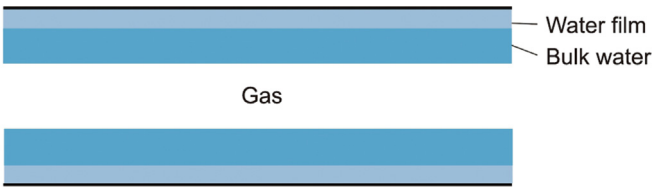

Fig. 13. Divided gas and water regions. Reproduced from Ref. [114] with permission.

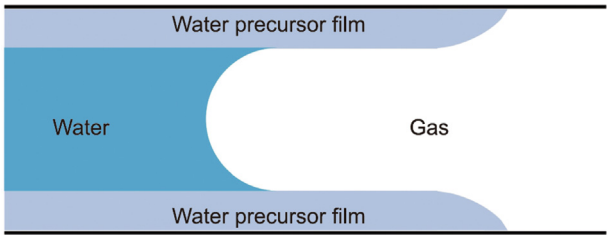

Fig. 14. Divided gas, water, and precursor film regions. Reproduced from Ref. [115] with permission.

where L_t is the spontaneous imbibition distance; L_f is the meniscus length along the precursor film; and ρ_i and ρ_b are the densities for the interfacial and bulk fluids, respectively.

In addition, to incorporate the influence of the dynamic contact angle, Tian et al. [116] properly modified the capillary pressure (p_c) equation, as shown in Eq. (16):

$$p_c = \frac{2\gamma_{ow}}{\beta R_{eq}}\cos\theta_d \quad \text{with} \quad \cos\theta_d = \cos\theta_{eq} - \alpha Ca \tag{16}$$

where γ_{ow} is the interfacial tension; β is the dimensionless geometrical factor; R_{eq} is the effective pore radius; θ_{eq} and θ_d are the equilibrium and dynamic contact angles, respectively; α is the molecular interaction constant; and Ca is the capillary number.

Furthermore, the authors derived a more comprehensive model to describe the fluid dynamics at the nanoscale, including interfacial forces, inertial effects and others; see Eq. (17).

$$p_c + \Delta p = p_e + p_v + p_a + p_g + p_f \tag{17}$$

$$p_f = \frac{2\zeta}{R}v \tag{18}$$

$$v = \gamma_{ow}(\cos\theta_{eq} - \cos\theta_d)/\zeta \tag{19}$$

where p_e is the capillary end effect; p_v is the inertial term; p_a is the viscous term; p_g is the gravitational term; p_f is the friction term; ζ is the contact line friction coefficient; R is the pore radius; and v is the spontaneous imbibition rate.

3.3. Simulation

To date, many numerical simulations on multi-phase flow at the nanoscale have been reported. Liu et al. [117] investigated the physics of H_2O–CH_4 two-phase flow in hydrophilic quartz nanopores (with a 10 nm width). The simulation results demonstrated that ① water tends to form a water film; ② at low pressure, a water film–CH_4–water film sandwich structure can form; and ③ at high pressure, CH_4 mainly exists in a gas bubble state surrounded by water. Surprisingly, a linear Darcy's law can be used to describe the abovementioned physics, which is attributed to the disappearance of the slip effect caused by gas–water friction. However, this hypothesis has not yet been validated by experiments. Xu et al. [118] studied the effect of wettability on H_2O–CH_4 two-phase flow in nanopores with a pore size of 6 nm (Fig. 15). The simulation results indicated that water molecules tend to form a water film to cover the hydrophilic pore surface, thus suppressing the gas slip flow and shifting the flow into viscous flow. In contrast, water molecules tend to accumulate together to form clusters inside the hydrophobic nanopores, and the slip effect will be dominant. These results are qualitatively consistent with the MD simulation results of Zhang et al. [119].

Gong et al. [120] investigated the effect of water saturation on CH_4 adsorption on the kerogen surface. The results indicated that the CH_4 adsorption capacity decreased from 1.2 to 0.6 mmol·g^{-1}

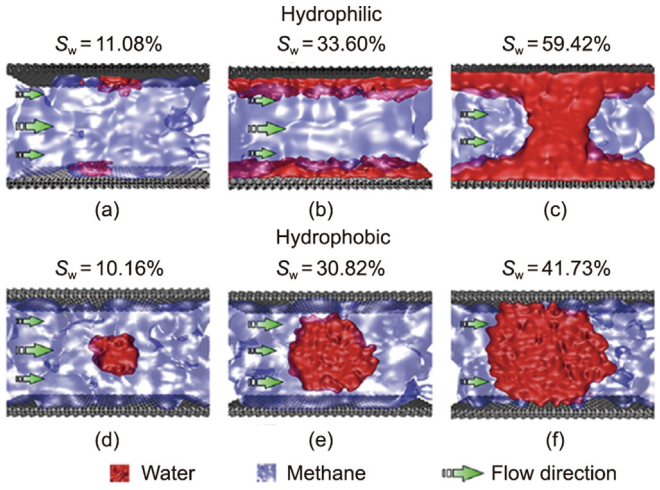

Fig. 15. Effect of wettability on H_2O–CH_4 two-phase flow in nanopores with a pore size of 6 nm. S_w: water saturation. Reproduced from Ref. [118] with permission.

with increasing water content. The work of Zhan et al. [121] on the molecular simulation of oil–water two-phase flow in quartz nanopores produced a new hydrodynamic flow model considering the fluid distributions, heterogeneous fluid properties, liquid–wall interactions, and liquid–liquid slip. They noted that the enhancement of oil flow due to liquid–liquid slip in nanopores cannot be ignored. Furthermore, Zhang et al. [122] investigated water–C8 and water–C10 two-phase flow in a calcite nanopore with a radius of 5 nm. At low water saturation, a water–oil–water layered structure was formed, while at high water saturation, a water bridge appeared. In addition, the front velocity had a piston-like profile (instead of a parabolic profile); thus, slip flow probably plays a role herein, which contradicts the classic Darcy flow, consistent with other MD simulations [123,124]. Ho and Wang [125] examined the velocity characteristics of the C8–scCO_2–H_2O (sc: super critical) mixture inside hydrophilic mica and hydrophobic kerogen. In hydrophilic nanopores, scCO_2 and water can absorb onto the surface, while C8 is located in the center. In hydrophobic nanopores, water has no influence on C8 mobility, while CO_2 can mix with C8 to reduce its viscosity and increase its flow rate. Considering the multicomponent characteristics of crude oil, Xu et al. [126] compared the dynamics of H_2O–C10 and H_2O–C3 + C6 + C10 inside a quartz nanopore. For the former system, a classic water slip flow was predicted, and the CH_4 flow rate was increased by 20%; for the latter system, up to a 5 $m \cdot s^{-1}$ slip velocity was observed. However, the fundamental reason was not provided in this work [126].

Ghazimirsaeed et al. [127] conducted a finite-volume-method numerical simulation of the droplet-based chemical bioreaction in a microreactor. The microchannels were serpentine and designed to be trapezoidal, triangular, and circular to study the effect of the aspect ratio. The results showed that the rectangular microchannel is the most useful. Chemical reactive flow is also common in formation acidification. Jia et al. [128,129] established a two-scale continuum model to calculate the mass conversion between solid and liquid phases and employed the Naiver–Stokes–Darcy equation to describe fluid flow. The model can be used to analyze a 2D acidizing process [130]. Their simulation results showed that the model can give a reasonable optimum acid injection rate and present typical dissolution patterns.

4. Research gaps and future outlook

Based on the abovementioned discussions, some gaps currently exist as follows:

(1) Current experimental investigations mainly use engineering and/or natural (nano)porous materials as media. However, engineering materials are usually unable to bear high pressure conditions, while natural rocks are usually heterogeneous. Thus, so far, experimentally, rigorous investigation of the fluid flow at the nanoscale has been impossible. Another challenge is to monitor the dynamics with high frequency and resolution. Moreover, experimental study of three-phase flow at the nanoscale is still lacking at present. Artificial nanoscale models cannot fully reflect the real situation, and their scales are difficult to diversify.

(2) Currently, theoretical studies are mainly conducted through modification of the equations or boundary conditions. However, thus far, whether the continuity assumption is valid remains uncertain. Many studies have provided control equations (Nernst–Planck and Navier–Stokes equations) for electrokinetic flow, but obtaining analytical solutions is difficult. Furthermore, the atomic and interfacial forces must be physically considered in future studies.

(3) Currently, the most popular method to study this topic is MD simulations. However, these simulations almost cannot be validated by experiments. The wettability and slip effects still have large uncertainties. For multi-field problems, conventional numerical simulations still suffer from unstable convergence and high computational complexity.

To address these limitations and close the abovementioned gaps, the following works are suggested:

(1) More advanced techniques and instruments to measure fluid flow at the nanoscale should be developed, and more representative nanoporous materials that can withstand high pressure should be synthesized. The artificial micro/nanochannels should replicate real flow conditions and be as reusable as possible. These works are necessary to promote fundamental development of the fluid mechanics at nanoscale.

(2) The theory on fluid mechanics at nanoscale is still in its infancy. The multi-field coupling processes and mechanisms must be considered to complete this theory. Appropriate simplified conditions can be applied to search for general solutions to the flow control equations as much as possible to improve the application of theory.

(3) New numerical simulation techniques that consider the real nanoscale physics and interactions must be developed, and the fluid flow dynamics must be simulated under *in-situ* conditions. Advanced algorithms can be explored to improve numerical simulation methods, reduce the time consumption, and improve the accuracy.

5. Conclusions

Fluid flow at nanoscale is closely related to nature and technology. This paper has systematically reviewed single- and multiphases flow at nanoscale in terms of experiments, theory and simulation. The following conclusions are drawn:

(1) Experiments, theory and simulations all demonstrated that the H–P equation is invalid for single-phase flow at the nanoscale; and the relationship among the slip length, shear rate, and wettability has been given. Appropriate modifications to the fluid viscosity, momentum equation and boundary conditions to include the interfacial interactions can be made.

(2) Wettability is an important parameter that plays a role in fluid flow at nanoscale. A hydrophilic nanopore surface reduces fluid flow, while a hydrophobic nanopore surface enhances fluid flow.

(3) Gas–water and oil–water two-phase flows at the nanoscale are strongly influenced by fluid–solid interactions; thus, nonlinear characteristics are obvious, for example, the TPG dramatically

increases and a stagnant adsorption layer forms on the nanopore surface. For the oil–water two-phase system, the front profile is piston-like instead of parabolic, which is caused by slip flow.

These insights will promote the significant development of nonlinear fluid mechanics and will provide important guidance for the relevant areas in nature and technology.

Compliance with ethics guidelines

Weiyao Zhu, Bin Pan, Zhen Chen, Wengang Bu, Qipeng Ma, Kai Liu, and Ming Yue declare that they have no conflict of interests or financial conflicts to disclose.

Acknowledgments

Weiyao Zhu thanks the funding support from the National Natural Science Foundation of China (51974013 and 11372033) and Open Research Foundation (NEPU-EOR-2019-003). Bin Pan thanks the initiative funding from the University of Science and Technology Beijing.

References

[1] Pan B, Clarkson CR, Younis A, Song C, Debuhr C, Ghanizadeh A, et al. New methods to evaluate impacts of osmotic pressure and surfactant on fracturing fluid loss and effect of contact angle on spontaneous imbibition data scaling in unconventional reservoirs. Fuel 2022;328:125328.
[2] Pan B, Clarkson CR, Debuhr C, Younis A, Song C, Ghanizadeh A, et al. Low-permeability reservoir sample wettability characterization at multiple scales: pore-, micro- and macro-contact angles. J Nat Gas Sci Eng 2021;95:104229.
[3] Gao Y, Wu K, Chen Z, Zhou T, Li J, Feng D, et al. Effect of wetting hysteresis on fluid flow in shale oil reservoirs. Energy Fuels 2021;35(15):12075–82.
[4] Li R, Chen Z, Wu K, Hao X, Xu J. An analytical model for water–oil two-phase flow in inorganic nanopores in shale oil reservoirs. Petrol Sci 2021;18(6):1776–87.
[5] Yang Y, Wang K, Zhang L, Sun H, Zhang K, Ma J. Pore-scale simulation of shale oil flow based on pore network model. Fuel 2019;251:683–92.
[6] Yang Y, Liu J, Yao J, Kou J, Li Z, Wu T, et al. Adsorption behaviors of shale oil in kerogen slit by molecular simulation. Chem Eng J 2020;387:124054.
[7] Alvarez JO, Schechter DS. Wettability alteration and spontaneous imbibition in unconventional liquid reservoirs by surfactant additives. SPE Reservoir Eval Eng 2017;20(01):107–17.
[8] Zhu W, Chen Z, Song Z, Wu J, Li W, Yue M. Research progress in theories and technologies of shale gas development in China. J Univ Sci Technol Beijing 2021;43:1397–412. Chinese.
[9] Chu H, Liao X, Chen Z, Lee WJJ. Rate-transient analysis of a constant-bottomhole-pressure multihorizontal well pad with a semianalytical single-phase method. SPE J 2020;25(06):3280–99.
[10] Chu H, Liao X, Chen Z, Zhao X, Liu W, Dong P. Transient pressure analysis of a horizontal well with multiple, arbitrarily shaped horizontal fractures. J Petrol Sci Eng 2019;180:631–42.
[11] Virkutyt J, Sillanpää M, Latostenmaa P. Electrokinetic soil remediation-critical overview. Sci Total Environ 2002;289(1–3):97–121.
[12] Aranda R, Davarzani H, Colombano S, Laurent F, Bertin H. Experimental study of foam flow in highly permeable porous media for soil remediation. Transp Porous Media 2020;134(1):231–47.
[13] Wang X, Ren L, Long T, Geng C, Tian X. Migration and remediation of organic liquid pollutants in porous soils and sedimentary rocks: a review. Environ Chem Lett 2023;21(1):479–96.
[14] Pan B, Li Y, Wang H, Jones F, Iglauer S. CO_2 and CH_4 wettabilities of organic-rich shale. Energy Fuels 2018;32(2):1914–22.
[15] Pan B, Jones F, Huang Z, Yang Y, Li Y, Hejazi SH, et al. Methane (CH_4) wettability of clay-coated quartz at reservoir conditions. Energy Fuels 2019;33(2):788–95.
[16] Pan B, Yin X, Ju Y, Iglauer S. Underground hydrogen storage: influencing parameters and future outlook. Adv Colloid Interface Sci 2021;294:102473.
[17] Pan B, Yin X, Zhu W, Yang Y, Ju Y, Yuan Y, et al. Theoretical study of brine secondary imbibition in sandstone reservoirs: implications for H_2, CH_4, and CO_2 geo-storage. Int J Hydrogen Energy 2022;47(41):18058–66.
[18] Pan B, Liu K, Ren B, Zhang M, Ju Y, Gu J, et al. Impacts of relative permeability hysteresis, wettability, and injection/withdrawal schemes on underground hydrogen storage in saline aquifers. Fuel 2023;333:126516.
[19] Iglauer S, Paluszny A, Pentland CH, Blunt MJ. Residual CO_2 imaged with X-ray micro-tomography. Geophys Res Lett 2011;38(21):L21403.
[20] Rezaei A, Hassanpouryouzband A, Molnar I, Derikvand Z, Haszeldine RS, Edlmann K. Relative permeability of hydrogen and aqueous brines in sandstones and carbonates at reservoir conditions. Geophys Res Lett 2022;49(12):e2022GL099433.
[21] Heinemann N, Alcalde J, Miocic JM, Hangx SJT, Kallmeyer J, Ostertag-Henning C, et al. Enabling large-scale hydrogen storage in porous media—the scientific challenges. Energy Environ Sci 2021;14(2):853–64.
[22] Jin X, Chao C, Edlmann K, Fan X. Understanding the interplay of capillary and viscous forces in CO_2 core flooding experiments. J Hydrol 2022;606:127411.
[23] Anderson R, Zhang L, Ding Y, Blanco M, Bi X, Wilkinson DP. A critical review of two-phase flow in gas flow channels of proton exchange membrane fuel cells. J Power Sources 2010;195(15):4531–53.
[24] Jeon DH. Wettability in electrodes and its impact on the performance of lithium-ion batteries. Energy Storage Mater 2019;18:139–47.
[25] Lian C, Su H, Li C, Liu H, Wu J. Non-negligible roles of pore size distribution on electroosmotic flow in nanoporous materials. ACS Nano 2019;13(7):8185–92.
[26] Cooley M, Sarode A, Hoore M, Fedosov DA, Mitragotri S, Sen GA. Influence of particle size and shape on their margination and wall-adhesion: implications in drug delivery vehicle design across nano-to-micro scale. Nanoscale 2018;10(32):15350–64.
[27] Müller K, Fedosov DA, Gompper G. Margination of micro- and nano-particles in blood flow and its effect on drug delivery. Sci Rep 2014;4:4871.
[28] Alkhadra MA, Su X, Suss ME, Tian H, Guyes EN, Shocron AN, et al. Electrochemical methods for water purification, ion separations, and energy conversion. Chem Rev 2022;122(16):13547–635.
[29] Sood A, Poletayev AD, Cogswell DA, Csernica PM, Mefford JT, Fraggedakis D, et al. Electrochemical ion insertion from the atomic to the device scale. Nat Rev Mater 2021;6(9):847–67.
[30] Suss ME, Porada S, Sun X, Biesheuvel PM, Yoon J, Presser V. Water desalination via capacitive deionization: what is it and what can we expect from it? Energy Environ Sci 2015;8(8):2296–319.
[31] Kenis PJA, Ismagilov RF, Takayama S, Whitesides GM, Li S, White HS. Fabrication inside microchannels using fluid flow. Acc Chem Res 2000;33(12):841–7.
[32] Battat S, Weitz DA, Whitesides GM. Nonlinear phenomena in microfluidics. Chem Rev 2022;122(7):6921–37.
[33] Iijima S. Helical microtubules of graphitic carbon. Nature 1991;354(6348):56–8.
[34] Majumder M, Chopra N, Andrews R, Hinds BJ. Enhanced flow in carbon nanotubes. Nature 2005;438(7064):44.
[35] Skoulidas AI, Ackerman DM, Johnson JK, Sholl DS. Rapid transport of gases in carbon nanotubes. Phys Rev Lett 2002;89(18):185901.
[36] Holt JK, Park HG, Wang Y, Stadermann M, Artyukhin AB, Grigoropoulos CP, et al. Fast mass transport through sub-2-nanometer carbon nanotubes. Science 2006;312(5776):1034–7.
[37] Noy A, Park HG, Fornasiero F, Holt JK, Grigoropoulos CP, Bakajin O. Nanofluidics in carbon nanotubes. Nano Today 2007;2(6):22–9.
[38] Tofighy MA, Mohammadi T. Nickel ions removal from water by two different morphologies of induced CNTs in mullite pore channels as adsorptive membrane. Ceram Int 2015;41(4):5464–72.
[39] Wang Y, Zhu J, Huang H, Cho HH. Carbon nanotube composite membranes for microfiltration of pharmaceuticals and personal care products: capabilities and potential mechanisms. J Membr Sci 2015;479:165–74.
[40] Zhong J, Zhao Y, Lu C, Xu Y, Jin Z, Mostowfi F, et al. Nanoscale phase measurement for the shale challenge: multicomponent fluids in multiscale volumes. Langmuir 2018;34(34):9927–35.
[41] Zhong J, Zandavi SH, Li H, Bao B, Persad AH, Mostowfi F, et al. Condensation in one-dimensional dead-end nanochannels. ACS Nano 2017;11(1):304–13.
[42] Sinton D. Energy: the microfluidic frontier. Lab Chip 2014;14(17):3127–34.
[43] Kong T, Shum HC, Weitz DA. The fourth decade of microfluidics. Small 2020;16(9):2000070.
[44] Whitesides GM. The origins and the future of microfluidics. Nature 2006;442(7101):368–73.
[45] Cui H, Li ZS, Zhu S. Flow characteristics of liquids in microtubes driven by a high pressure. Phys Fluids 2004;16(5):1803–10.
[46] Choi CH, Westin KJA, Breuer KS. Apparent slip flows in hydrophilic and hydrophobic microchannels. Phys Fluids 2003;15(10):2897–902.
[47] Lumma D, Best A, Gansen A, Feuillebois F, Rädler JO, Vinogradova OI. Flow profile near a wall measured by double-focus fluorescence cross-correlation. Phys Rev E 2003;67(5):056313.
[48] Jin S, Huang P, Park J, Yoo JY, Breuer KS. Near-surface velocimetry using evanescent wave illumination. Exp Fluids 2004;37(6):825–33.
[49] Horn RG, Vinogradova OI, Mackay ME, Phan-Thien N. Hydrodynamic slippage inferred from thin film drainage measurements in a solution of nonadsorbing polymer. J Chem Phys 2000;112(14):6424–33.
[50] Shen W, Song F, Hu X, Zhu G, Zhu W. Experimental study on flow characteristics of gas transport in micro- and nanoscale pores. Sci Rep 2019;9(1):10196.
[51] Nordberg ME. Properties of some Vycor-brand glasses. J Am Ceram Soc 1944;27(10):299–305.
[52] Debye P, Cleland RL. Flow of liquid hydrocarbons in porous vycor. J Appl Phys 1959;30(6):843–9.
[53] Gruener S, Wallacher D, Greulich S, Busch M, Huber P. Hydraulic transport across hydrophilic and hydrophobic nanopores: flow experiments with water and *n*-hexane. Phys Rev E 2016;93(1):013102.
[54] You XY, Zheng JR, Jing Q. Effects of boundary slip and apparent viscosity on the stability of microchannel flow. Forsch Im Ingenieurwes 2007;71:99–106.
[55] Wang XF, Zhu WY, Deng QJ, Zhang XL, Lou L, Gao Y. Micro circular tube flow mathematical model with the effect of van der Waals force. Appl Mech Mat 2014;448–453:975–81.

[56] Thomas JA, McGaughey AJH. Reassessing fast water transport through carbon nanotubes. Nano Lett 2008;8(9):2788–93.
[57] Wu K, Chen Z, Li J, Li X, Xu J, Dong X. Wettability effect on nanoconfined water flow. Proc Natl Acad Sci USA 2017;114(13):3358–63.
[58] Zhang L, Wu K, Chen Z, Li J, Yu X, Yang S, et al. Quasi-continuum water flow under nanoconfined conditions: coupling the effective viscosity and the slip length. Ind Eng Chem Res 2020;59(46):20504–14.
[59] Zhang X, Zhu W, Cai Q, Liu Q, Wang X, Lou Y. Analysis of weakly compressible fluid flow in nano/micro-size circular tubes considering solid wall force. J Univ Sci Technol Beijing 2014;36:569–75. Chinese.
[60] Zhang X, Zhu W, Cai Q, Shi Y, Wu X, Jin T, et al. Compressible liquid flow in nano- or micro-sized circular tubes considering wall–liquid Lifshitz–van der Waals interaction. Phys Fluids 2018;30(6):062002.
[61] Heinbuch U, Fischer J. Liquid flow in pores: slip, no-slip, or multilayer sticking. Phys Rev A Gen Phys 1989;40(2):1144–6.
[62] Thompson PA, Troian SM. A general boundary condition for liquid flow at solid surfaces. Nature 1997;389(6649):360–2.
[63] Davidson C, Xuan X. Electrokinetic energy conversion in slip nanochannels. J Power Sources 2008;179(1):297–300.
[64] Jeong M, Kim Y, Zhou W, Tao WQ, Ha MY. Effects of surface wettability, roughness and moving wall velocity on the Couette flow in nano-channel using multi-scale hybrid method. Comput Fluids 2017;147:1–11.
[65] Huang DM, Sendner C, Horinek D, Netz RR, Bocquet L. Water slippage versus contact angle: a quasiuniversal relationship. Phys Rev Lett 2008; 101(22):226101.
[66] Hanasaki I, Nakatani A. Flow structure of water in carbon nanotubes: poiseuille type or plug-like? J Chem Phys 2006;124(14):144708.
[67] Joseph S, Aluru NR. Why are carbon nanotubes fast transporters of water? Nano Lett 2008;8(2):452–8.
[68] Wang S, Javadpour F, Feng Q. Molecular dynamics simulations of oil transport through inorganic nanopores in shale. Fuel 2016;171:74–86.
[69] Wang S, Feng Q, Javadpour F, Yang YB. Breakdown of fast mass transport of methane through calcite nanopores. J Phys Chem C 2016;120(26):14260–9.
[70] Wu K, Chen Z, Li J, Xu J, Wang K, Wang S, et al. Manipulating the flow of nanoconfined water by temperature stimulation. Angew Chem 2018;57 (28):8432–7.
[71] Movahed S, Li D. Electrokinetic transport through nanochannels. Electrophoresis 2011;32(11):1259–67.
[72] Han W, Chen X. Nano-electrokinetic ion enrichment of highly viscous fluids in micro-nanochannel. Chem Eng Process 2019;143:107626.
[73] Hsu WL, Harvie DJE, Davidson MR, Dunstan DE, Hwang J, Daiguji H. Viscoelectric effects in nanochannel electrokinetics. J Phys Chem C 2017;121(37):20517–23.
[74] Mo X, Hu X. Electroviscous effect on pressure driven flow and related heat transfer in microchannels with surface chemical reaction. Int J Heat Mass Transf 2019;130:813–20.
[75] Li C, Liu Z, Qiao N, Feng Z, Tian ZQ. The electroviscous effect in nanochannels with overlapping electric double layers considering the height size effect on surface charge. Electrochim Acta 2022;419:140421.
[76] Zhang M, Zhan S, Jin Z. Recovery mechanisms of hydrocarbon mixtures in organic and inorganic nanopores during pressure drawdown and CO_2 injection from molecular perspectives. Chem Eng J 2020;382:122808.
[77] Li J, Sun C. Molecular insights on competitive adsorption and enhanced displacement effects of CO_2/CH_4 in coal for low-carbon energy technologies. Energy 2022;261:125176.
[78] Hong X, Yu H, Xu H, Wang X, Jin X, Wu H, et al. Competitive adsorption of asphaltene and *n*-heptane on quartz surfaces and its effect on crude oil transport through nanopores. J Mol Liq 2022;359:119312.
[79] Brunauer S, Deming LS, Deming WE, Teller E. On a theory of the van der Waals adsorption of gases. J Am Chem Soc 1940;62(7):1723–32.
[80] Gregg S, Sing K. Adsorption, surface area and porosity. 2nd ed. London: Academic Press; 1982.
[81] Rani S, Padmanabhan E, Prusty BK. Review of gas adsorption in shales for enhanced methane recovery and CO_2 storage. J Petrol Sci Eng 2019;175:634–43.
[82] Wu T, Zhang D. Impact of adsorption on gas transport in nanopores. Sci Rep 2016;6:23629.
[83] Ali A, Le TTB, Striolo A, Cole DR. Salt effects on the structure and dynamics of interfacial water on calcite probed by equilibrium molecular dynamics simulations. J Phys Chem C 2020;124(45):24822–36.
[84] Zhang M, Li W, Jin Z. Structural properties of deprotonated naphthenic acids immersed in water in pristine and hydroxylated carbon nanopores from molecular perspectives. J Hazard Mater 2021;415:125660.
[85] Han A, Mondin G, Hegelbach NG, de Rooij NF, Staufer U. Filling kinetics of liquids in nanochannels as narrow as 27 nm by capillary force. J Colloid Interface Sci 2006;293(1):151–7.
[86] Li B, Zhu W, Ma Q, Li H, Kong D, Song Z. Pore-scale visual investigation on the spontaneous imbibition of surfactant solution in oil-wet capillary tubes. Energy Sources Part A 2022;44(2):3395–405.
[87] Huber P, Grüner S, Schäfer C, Knorr K, Kityk AV. Rheology of liquids in nanopores: a study on the capillary rise of water, *n*-Hexadecane and *n*-Tetracosane in mesoporous silica. Eur Phys J Spec Top 2007;141(1):101–5.
[88] Gruener S, Huber P. Spontaneous imbibition dynamics of an *n*-alkane in nanopores: evidence of meniscus freezing and monolayer sticking. Phys Rev Lett 2009;103(17):174501.
[89] Gruener S, Hermes HE, Schillinger B, Egelhaaf SU, Huber P. Capillary rise dynamics of liquid hydrocarbons in mesoporous silica as explored by gravimetry, optical and neutron imaging: nano-rheology and determination of pore size distributions from the shape of imbibition fronts. Colloids Surf A Physicochem Eng Asp 2016;496:13–27.
[90] Pan B, Clarkson CR, Atwa M, Debuhr C, Ghanizadeh A, Birss VI. Wetting dynamics of nanoliter water droplets in nanoporous media. J Colloid Interface Sci 2021;589:411–23.
[91] Pan B, Clarkson CR, Atwa M, Tong X, Debuhr C, Ghanizadeh A, et al. Spontaneous imbibition dynamics of liquids in partially-wet nanoporous media: experiment and theory. Transp Porous Media 2021;137(3):555–74.
[92] Gogotsi Y, Libera JA, Güvenç-Yazicioglu A, Megaridis CM. *In situ* multiphase fluid experiments in hydrothermal carbon nanotubes. Appl Phys Lett 2001; 79(7):1021–3.
[93] Rossi MP, Ye H, Gogotsi Y, Babu S, Ndungu P, Bradley JC. Environmental scanning electron microscopy study of water in carbon nanopipes. Nano Lett 2004;4:989–93.
[94] Anand U, Ghosh T, Aabdin Z, Koneti S, Xu X, Holsteyns F, et al. Dynamics of thin precursor film in wetting of nanopatterned surfaces. Proc Natl Acad Sci USA 2021;118(38):e2108074118.
[95] Fu L, Zhai J. Biomimetic stimuli-responsive nanochannels and their applications. Electrophoresis 2019;40(16–17):2058–74.
[96] Ferrati S, Fine D, You J, De Rosa E, Hudson L, Zabre E, et al. Leveraging nanochannels for universal, zero-order drug delivery *in vivo*. J Control Release 2013;172(3):1011–9.
[97] Romano-Feinholz S, Salazar-Ramiro A, Muñoz-Sandoval E, Magaña-Maldonado R, Hernández Pedro N, Rangel López E, et al. Cytotoxicity induced by carbon nanotubes in experimental malignant glioma. Int J Nanomed 2017;12:6005–26.
[98] Ly KL, Hu P, Pham LHP, Luo X. Flow-assembled chitosan membranes in microfluidics: recent advances and applications. J Mater Chem B Mater Biol Med 2021;9(15):3258–83.
[99] Shakeri A, Sun N, Badv M, Didar TF. Generating 2-dimensional concentration gradients of biomolecules using a simple microfluidic design. Biomicrofluidics 2017;11(4):044111.
[100] Gu Y, Hegde V, Bishop KJM. Measurement and mitigation of free convection in microfluidic gradient generators. Lab Chip 2018;18(22):3371–8.
[101] Wang L, Parsa E, Gao Y, Ok JT, Neeves K, Yin X, et al. Experimental study and modeling of the effect of nanoconfinement on hydrocarbon phase behavior in unconventional reservoirs. In: Proceedings of the SPE Western North American and Rocky Mountain Joint Meeting; 2014 Apr 17–18; Denver, CO, USA. Richardson: OnePetro; 2014.
[102] Akbarabadi M, Saraji S, Piri M, Georgi D, Delshad M. Nano-scale experimental investigation of *in-situ* wettability and spontaneous imbibition in ultra-tight reservoir rocks. Adv Water Resour 2017;107:160–79.
[103] Xu K, Liang T, Zhu P, Qi P, Lu J, Huh C, et al. A 2.5-D glass micromodel for investigation of multi-phase flow in porous media. Lab Chip 2017; 17(4):640–6.
[104] Deglint HJ, Clarkson CR, Ghanizadeh A, DeBuhr C, Wood JM. Comparison of micro- and macro-wettability measurements and evaluation of micro-scale imbibition rates for unconventional reservoirs: implications for modeling multi-phase flow at the micro-scale. J Nat Gas Sci Eng 2019;62:38–67.
[105] Qiao J, Zeng J, Jiang S, Yang G, Zhang Y, Feng X, et al. Investigation on the unsteady-state two-phase fluid transport in the nano-pore system of natural tight porous media. J Hydrol 2022;607:127516.
[106] Sheng JJ. Critical review of field EOR projects in shale and tight reservoirs. J Petrol Sci Eng 2017;159:654–65.
[107] Zhou Z, Li X, Teklu TW. A critical review of osmosis-associated imbibition in unconventional formations. Energies 2021;14(4):835.
[108] Pan B, Clarkson CR, Younis A, Song C, Debuhr C, Ghanizadeh A, et al. Fracturing fluid loss in unconventional reservoirs: evaluating the impact of osmotic pressure and surfactant and methods to upscale results. In: Proceedings of the SPE/AAPG/SEG Unconventional Resources Technology Conference (URTeC); 2021 Jul 26–28; Houston, TX, USA. Houston: Society of Exploration Geophysicists; 2021. p. 3773.
[109] Zhu W, Liu Y, Shi Y, Zou G, Zhang Q, Kong D. Effect of dynamic threshold pressure gradient on production performance in water-bearing tight gas reservoir. Adv GeoEnergy Res 2022;6(4):286–95.
[110] Zhu W, Zou G, Liu Y, Liu W, Pan B. The influence of movable water on the gas-phase threshold pressure gradient in tight gas reservoirs. Energies 2022;15:5309.
[111] Jacob B. Dynamics of fluids in porous media. 5th ed. New York City: Dover Publications; 2013.
[112] Zhu W. Study on the theory of multiphase mixed seepage in porous media. J Univ Sci Technol Beijing 2023;45(5):833–9. Chinese.
[113] Zhang X. Percolatiton theory research of weekly compressible fluid flow considering wall–liquid interaction [dissertation]. Beijing: University of Science and Technology Beijing; 2014. Chinese.

[114] Wang X. Study on micro flow dynamics mechanisms and numerical simulation in porous media [dissertation]. Beijing: University of Science and Technology Beijing; 2009. Chinese.
[115] Zhang L, Yu X, Chen Z, Li J, Hui G, Yang M, et al. Capillary dynamics of confined water in nanopores: the impact of precursor films. Chem Eng J 2021;409:128113.
[116] Tian W, Wu K, Chen Z, Lai L, Gao Y, Li J. Effect of dynamic contact angle on spontaneous capillary–liquid–liquid imbibition by molecular kinetic theory. SPE J 2021;26(04):2324–39.
[117] Liu B, Qi C, Zhao X, Teng G, Zhao L, Zheng H, et al. Nanoscale two-phase flow of methane and water in shale inorganic matrix. J Phys Chem C 2018;122 (46):26671–9.
[118] Xu H, Yu H, Fan J, Zhu Y, Wang F, Wu H. Two-phase transport characteristic of shale gas and water through hydrophilic and hydrophobic nanopores. Energy Fuels 2020;34(4):4407–20.
[119] Zhang L, Li Q, Liu C, Liu Y, Cai S, Wang S, et al. Molecular insight of flow property for gas–water mixture (CO_2/CH_4–H_2O) in shale organic matrix. Fuel 2021;288:119720.
[120] Gong L, Shi JH, Ding B, Huang ZQ, Sun SY, Yao J. Molecular insight on competitive adsorption and diffusion characteristics of shale gas in water-bearing channels. Fuel 2020;278:118406.
[121] Zhan S, Su Y, Jin Z, Zhang M, Wang W, Hao Y, et al. Study of liquid–liquid two-phase flow in hydrophilic nanochannels by molecular simulations and theoretical modeling. Chem Eng J 2020;395:125053.
[122] Zhang W, Feng Q, Jin Z, Xing X, Wang S. Molecular simulation study of oil–water two-phase fluid transport in shale inorganic nanopores. Chem Eng Sci 2021;245:116948.
[123] Galliero G. Lennard-Jones fluid–fluid interfaces under shear. Phys Rev E 2010;81(5):056306.
[124] Koplik J, Banavar JR. Slip, immiscibility, and boundary conditions at the liquid–liquid interface. Phys Rev Lett 2006;96(4):044505.
[125] Ho TA, Wang Y. Enhancement of oil flow in shale nanopores by manipulating friction and viscosity. Phys Chem Chem Phys 2019;21(24):12777–86.
[126] Xu J, Zhan S, Wang W, Su Y, Wang H. Molecular dynamics simulations of two-phase flow of *n*-alkanes with water in quartz nanopores. Chem Eng J 2022;430:132800.
[127] Ghazimirsaeed E, Madadelahi M, Dizani M, Shamloo A. Secondary flows, mixing, and chemical reaction analysis of droplet-based flow inside serpentine microchannels with different cross sections. Langmuir 2021;37(17):5118–30.
[128] Jia C, Huang Z, Sepehrnoori K, Yao J. Modification of two-scale continuum model and numerical studies for carbonate matrix acidizing. J Petrol Sci Eng 2021;197:107972.
[129] Jia C, Sepehrnoori K, Huang Z, Zhang H, Yao J. Numerical studies and analysis on reactive flow in carbonate matrix acidizing. J Petrol Sci Eng 2021;201:108487.
[130] Jia C, Sepehrnoori K, Huang Z, Yao J. Modeling and analysis of carbonate matrix acidizing using a new two-scale continuum model. SPE J 2021; 26(05):2570–99.